




<b>Title:</b>	Non-invasive quantification of pressure drops in stenotic intracranial vessels: using deep learning-enhanced 4D flow MRI to characterize the regional haemodynamics of the pulsing brain
<b>Author(s):</b>	El Ahmar A., Schnell S., Ansari S. A., Abdalla R. N., Vali A., Aristova M., Markl M., Winter P., Marlevi D.
<b>First published:</b>	2025
<b>Type of publication:</b>	Journal article
<b>Published version:</b>	Postprint Version
<b>This version is available at:</b>	<a href="https://nbn-resolving.org/urn:nbn:de:gbv:9-opus-131782">https://nbn-resolving.org/urn:nbn:de:gbv:9-opus-131782</a>
<b>Citation details:</b>	This is the peer reviewed version of the following article:  El Ahmar A., Schnell S., Ansari S. A., Abdalla R. N., Vali A., Aristova M., Markl M., Winter P., Marlevi D. 2025. Non-invasive quantification of pressure drops in stenotic intracranial vessels: using deep learningenhanced 4D flow MRI to characterize the regional haemodynamics of the pulsing brain. <i>Interface Focus</i> 15: 20240040, which has been published in final form at <a href="https://doi.org/10.1098/rsfs.2024.0040">https://doi.org/10.1098/rsfs.2024.0040</a>
<b>Licence:</b>	 <a href="https://creativecommons.org/licenses/by/4.0/">Creative Commons - Attribution 4.0 International</a>

# *Non-invasive Quantification of Pressure Drops in Stenotic Intracranial Vessels - Using Deep-Learning Enhanced 4D Flow MRI to Characterize the Regional Hemodynamics of the Pulsing Brain*

**Ali El Ahmar<sup>1\*</sup>, Susanne Schnell<sup>1,2\*</sup>, Sameer A. Ansari<sup>2,3</sup>, Ramez N. Abdalla<sup>2</sup>, Alireza Vali<sup>4</sup>, Maria Aristova<sup>3</sup>, Michael Markl<sup>2</sup>, Patrick Winter<sup>1,2†</sup> and David Marlevi<sup>5,6†</sup>**

\*: Equal contributing first authors.

†: Equal contributing last authors.

<sup>1</sup>Department of Medical Physics, Faculty of Mathematics and Natural Sciences, University of Greifswald, Greifswald, Germany

<sup>2</sup>Department of Radiology, Northwestern University, Feinberg School of Medicine, Chicago, IL, USA

<sup>3</sup>Department of Neurology and Neurological Surgery, Northwestern University, Feinberg School of Medicine, Chicago, IL, USA

<sup>4</sup>Qualcomm Technologies, Inc., San Diego, CA, USA

<sup>5</sup>Department of Molecular Medicine and Surgery, Karolinska Institutet, Stockholm, Sweden

<sup>6</sup>Institute for Medical Engineering and Sciences, Massachusetts Institute of Technology, Cambridge, MA, USA

Stenosis of major intracranial arteries is a significant cause of stroke, with assessment of trans-stenotic pressure drops being a key marker of functional stenosis severity. Non-invasive methods for quantifying intracranial pressure changes are hence crucial, however, the narrow and tortuous cerebrovascular network poses challenges to traditional assessment methods such as transcranial Doppler. This study investigates the use of novel deep learning-enhanced super-resolution 4D Flow MRI in combination with a physics-informed virtual work-energy relative pressure (vWERP) technique to quantify pressure drops across stenotic intracranial arteries. Performance was validated in intracranial-mimicking *in-vitro* experiments using pulsatile flow, before being transferred into an *in-vivo* cohort of patients with intracranial atherosclerotic disease. Conversion into sub-mm super-resolution imaging significantly improved the accuracy of regional relative pressure estimations in the pulsing brain arteries, mitigating biases observed at >1mm resolution imaging, and agreeing strongly with reference catheter-based invasive measures across both moderate and severe stenoses. The *in-vivo* analysis also revealed a significant increase in pressure drops when converting into sub-mm super-resolution data, underlining the importance of apparent image resolution in a clinical setting. The results highlight the potential of super-resolution 4D Flow MRI for non-invasive quantification of cerebrovascular pressure changes in pulsing intracranial arteries across stenotic vessel segments.

**Keywords:** Pulsing brain, trans-stenotic pressure drop, 4D Flow MRI, Super resolution, intracranial atherosclerotic disease

## 1. Introduction

Stenosis of the major intracranial arteries due to various cerebrovascular pathologies is a major cause of ischemic stroke (1–3). Whereas assessment of the degree of stenosis represents an anatomical standard grading of intraluminal protrusion, its direct relation to future cardiovascular events remains under debate (4). Instead, assessment of the trans-stenotic pressure

drop within the pulsing vessel serves as a more direct indicator of a lesion's functional severity, where elevated drops in pressure indicate a more regionally impaired hemodynamic setting (5). As such, measurements of vascular pressure drops have become a mainstay in various areas of vascular medicine, where certain treatment decisions are guided by the measured pressure drop across the stenosis (e.g., idiopathic intracranial hypertension (IIH) treatment through endovascular stenting of dural venous sinus stenosis (DVSS)) (6). Pressure drop at the stenosis helps to characterise the hemodynamic impact of a lesion and its clinical significance in patients with Intracranial atherosclerotic disease (ICAD) (7).

Within this space, catheter-based intravascular pressure measurement is considered the gold standard in assessing regional hemodynamics (8). However, its widespread application is restricted by the invasive nature of the procedure and safety profile (9,10). In particular, in the cerebrovascular field, arterial catheter-based pressure assessments have yet to receive regulatory approval and are so far only conducted in highly controlled research settings during interventional procedures (11,12).

As a non-invasive alternative, Doppler ultrasound enables the calculation of pressure drops by deriving them from measured flow velocities of the pulsing blood using the so-called Bernoulli equation (13). Following inherent methods assumptions, however, such Bernoulli-based estimates are known to differ from invasive measurements when applied in more complex vascular settings (14–16) and, in the brain in particular, inherent method biases have been reported (17). Further, whilst transcranial Doppler enables insight into regional sections of the cerebrovasculature (18), its use across a wider set of intracranial vessels is limited by the acoustically shielding cranium as well as the Ultrasonic window (19). In addition, it offers poor or even non-existent anatomical imaging (20).

Moving into full-field imaging, time-resolved four-dimensional phase-contrast magnetic resonance imaging (4D Flow MRI) is an acquisition technique enabling full volumetric blood flow quantification and has been used in several studies to investigate cerebrovascular flow dynamics (21,22). The access to complete blood flow velocity information of the pulsing brain arteries also enables the usage of higher-order pressure estimators, where intracranial pressure drops have been quantified across a number of studies (23–26). To exemplify, Vali et al used a reduced-form Bernoulli (RB) principle with 4D Flow MRI to estimate the pressure drop across atherosclerotic intracranial vessels, noting estimation biases (7). Alternatively, the use of a pressure Poisson equation (PPE) has been proposed for accessing pressure data from 4D Flow MRI (23,27–29). However, significant biases have been reported as a function of defined flow domain (14,30); a problem aggravated when moving into intracranial settings with regions of highly restricted or narrow flow (31,32). More recently, Marlevi et al presented the virtual work-energy relative pressure (vWERP) method to address some of the limitations in existing pressure estimation techniques (17,33), showcasing accurate behaviour across a variety of domains (17,33) including validation against invasive catheterisation data (33). Still, dependence on spatial resolution has been highlighted in the intracranial space. (17), leaving the assessment of pressure gradients through small diameter cerebrovascular vessels directly dependent on acquired, high image resolution.

The dependence on spatial resolution in intracranial vascular imaging of the pulsing blood flow is a direct effect of the complex network of small, tortuous, bifurcating vessels making up the cerebrovasculature. For the sake of 4D Flow MRI, imaging can be theoretically performed at increasingly fine spatial samplings, however, the direct trade-off between resolution, noise, and scan time often makes such imaging unfeasible in a clinical setting. Instead, in an effort to stay within existing imaging protocol times, deep learning methods have started to be employed in the 4D Flow MRI space to achieve improved resolution post-processing (using so-called *super-resolution* imaging) (34–36). A number of these efforts have also targeted intracranial applications, seeking improved flow visualisation and quantification (34). Herein, Ferdian et al. utilised a trained residual super-resolution network in conjunction with vWERP-based derivations to specifically achieve accurate pressure drop estimations across various intracranial, arterial vessel sections, overcoming inherent estimation biases observed at low-resolution network input (37,38).

Although this approach was validated in a patient-specific *in-silico* cohort, experimental validation of the utility of image-based super-resolution pressure gradient estimations remains to be explicitly performed.

Therefore, the aim of this study was to experimentally validate the use of super-resolution 4D Flow MRI and coupled vWERP pressure drop analysis in the pulsing tortuous brain arteries for the estimation of pressure changes in intracranial vessels, using a dedicated *in-vitro* experimental cerebrovascular flow model. As a complement to experimental validation, we also sought to extend the approach into an *in-vivo* clinical patient cohort with intracranial atherosclerotic stenosis, showcasing the utility and effectiveness of super-resolution imaging setup with direct clinical relevance.

## 2. Methods

### 2.1. *In-vitro* experiment

A 4-channel 24x12cm silicon phantom (39) was utilised for the *in-vitro* experiments. The phantom comprised three channels each with an 8 mm diameter: one without stenosis, one with 50% stenosis (narrowed to 4 mm), and one with 75% stenosis (narrowed to 2 mm), alongside a fourth 5 mm channel without stenosis (see Fig. 1) (39). The stenosis severity is consistent with the definition provided by the Warfarin-Aspirin Symptomatic Intracranial Disease (WASID) trial, where the degree of stenosis is determined by the diameter reduction (40).

The pulsatile flow (using the “Carotid” setting) was provided by a commercially available pump (CompuFlow 1000-MR pump, Shelley Medical Imaging Technologies, London, Canada) at a rate of 7.6 ml/s with 72 strokes/min. A coaxial cable with BNC (Bayonet Neill–Concelman) and RCA (Radio Corporation of America) connectors was used to convey a TTL (Transistor–transistor logic) external trigger signal from the pump console to trigger the cardiac-gated 4D Flow MRI acquisition.

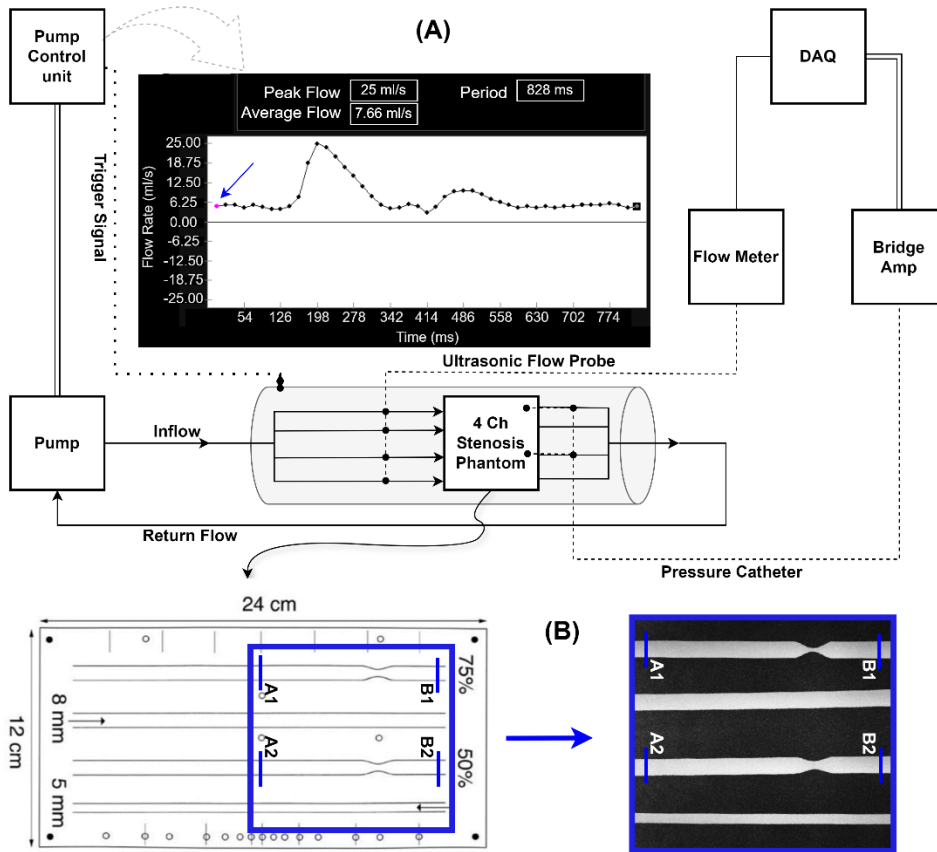


**FIGURE 1** (A) schematic of the experimental setup: The pump provided a pulsatile flow of 7.66 ml/s, and a period of 828 ms as shown in the graph. The pump control unit provided an external synchronisation trigger signal for the MRI (trigger point on the graph marked with a blue arrow). An ultrasonic flowmeter was used to measure the flow rate on the inlet of each channel. Additionally, the pressure within the phantom pre- and post of each stenosis was measured using a pressure catheter. Both measurements occurred outside the magnet room and were recorded via a data acquisition system (DAQ). (B) Left: Schematic representation of the silicone stenosis phantom, detailing dimensions and locations of pressure measurement planes. Right: Maximum intensity projection (MIP) images derived from 3D time-of-flight (TOF) MRI, also delineating the positions of pressure measurement planes (highlighted in light blue on both left and right images).

The circuit was filled with a blood-mimicking solution composed of 60% water and 40% glycerol, with a viscosity of 0.003 kg/(m·s) and an 1100 kg/m<sup>3</sup> density. Gadovist 0.1mol/ml (Bayer, Leverkusen, Germany) was introduced into this solution at a concentration of approximately 0.2% by volume to shorten  $T_1$  and thus enhance the MRI signal-to-noise ratio (SNR) (41).

To extract invasive reference data from the pulsing brain-artery-mimicking phantom setup, a SPR-330 Mikro-Tip<sup>®</sup> 3F pressure catheter (Millar Instruments, Houston, USA) connected to a PowerLab 16/35 data acquisition system (PowerLab, ADInstruments, Australia) was positioned at 2 distinct locations (see Fig. 1): upstream (A1/A2); downstream (B1/B2). The flow rate was measured at the inlet of each channel using the TS410 tubing module and ME 6PXL clamp-on Doppler ultrasound flow sensor (Transonic Systems Inc., Ithaca, USA).

The invasive catheter system used in this study was not MR-compatible; therefore, all measurements were conducted outside the magnet room. To ensure consistency, catheter measurements for the determination of relative pressure were performed without interrupting the pump, maintaining the same flow rate and waveform throughout.

For the assessment of pressure drops from the catheter measurements between two locations, two pressure waveforms (before and after stenosis) had to be extracted. Given measurement variability primarily resulting from catheter-induced errors, such as the absence of higher-frequency pressure oscillations and increased flow resistance caused by the presence of the catheter (42), the pulsatile pressure signal was averaged over 10 pumping cycles (i.e., heartbeats) to create an average pressure curve for the average cardiac cycle. This was achieved by using a threshold-based algorithm described previously (43,44). Temporal averaging and calculation of standard deviations were applied to the catheter measurements before and after the stenosis.

Since proximal and distal catheter measurements were acquired in a successive pull-back procedure, and TTL trigger signals were not recorded for the catheter measurements, temporal alignment was deemed necessary. To achieve this, both recorded pressure curves were temporally aligned in an additional post-processing step by using the cross-correlation function  $x_{corr}$  of MATLAB's signal processing toolbox (45,46). Finally, the pressure drop (difference in pressure before and after the stenosis) was calculated.

To compare the relative pressure values for individual pumping phases with the reference, the catheter measurements needed to be temporally aligned with the triggered 4D Flow measurements with cross-correlation, using the same technique described above and linear shifts. The maximum correlation value, indicating the highest similarity between the signals, is located to determine temporal misalignment. Signals are then adjusted accordingly for alignment, with validation and refinement conducted as necessary (45,46).

## 2.2. *In-vivo* intracranial atherosclerotic disease cohort

10 patients diagnosed with intracranial atherosclerotic disease who presented with intracranial stenoses were retrospectively recruited (7). The cohort comprised 8 male and 2 female patients aged 52 to 82 years ( $\pm 9$  years) and weighing 60-124 kg ( $\pm 19.8$  kg). The severity of the stenosis ranged from mild (1 case) to moderate (5 cases) and severe (4 cases). The definition of stenosis severity is as follows: stenoses less than 50% are categorised as mild, from 50% to 69% as moderate, and 70% and more as severe (7). The same cohort was previously described by Vali et al (7) where only those with stenosis affecting larger arteries (diameter  $>2$  mm) were included. According to (7), six patients were excluded for the following reasons: 2 patients had total vessel occlusion, 2 patients had insufficient coverage of the Circle of Willis (CoW), 1 patient had stenosis in the M2 segment of the MCA (small vessel  $<2$  mm), and 1 patient was excluded due to extreme velocity aliasing in the high-VENC acquisition, which could not be corrected post-scan. In Table 1 the patient demographics and intracranial stenosis descriptions are summarised for each subject.

## 2.3. MRI

All *in-vitro* scans were performed on a 3T MRI scanner (Siemens MAGNETOM VIDA, Erlangen, Germany) with a Small Ultra Flex 18-channel coil (Siemens, Erlangen, Germany) and an externally ECG-triggered GRAPPA-accelerated ( $R=2$ ) dual-VENC 4D Flow MRI sequence (47). The 4D Flow MRI sequence is using the balanced two-sided encoding scheme with minimal echo time (TE) (47). Additionally, a 3D time-of-flight (TOF) Gradient Echo sequence (spatial resolution: 0.5mm isotropic) was employed for segmentation. 4D Flow measurements were conducted with 0.5 and 1 mm isotropic spatial resolutions (Acquired High Resolution (AHR) and Acquired Low Resolution (ALR) successively). Details of all *in-vitro* scan parameters can be found in Table 2. To mitigate displacement errors and ensure accurate velocity measurements, we used a phantom setup that aligned the direction of maximal flow with the H-F-direction (head-foot), which was defined as readout direction.

For the *in-vivo* measurements, patients with atherosclerotic stenosis who had received dual-VENC 4D Flow MRI and 3D TOF MRI were retrospectively selected from an institutional review board (IRB) approved study (7). All participants underwent imaging in a 3T MRI scanner (Siemens MAGNETOM Skyra, Erlangen, Germany), using a 20-channel head/neck coil (Siemens, Erlangen, Germany), with an ECG-triggered intracranial k-t GRAPPA accelerated ( $R=5$ ) dual-VENC 4D Flow MRI sequence (47) alongside a high-resolution GRE 3D TOF sequence (TR: 21 ms, TE: 3.24 ms, FA: 17°, voxel size:  $0.52 \times 0.52 \times 0.5$  mm<sup>3</sup> (interpolated to  $0.26 \times 0.26 \times 0.5$  mm<sup>3</sup>)) (7). Details of *in-vivo* scan parameters can be found in Table 2 (7). To minimise artefacts caused by pulsations of the eye fluid, a right-left (R-L) phase encoding direction was used during the 4D Flow scans resulting in motion artefacts also in right-left directions not interfering with the anatomy of interest.

## 2.4. Post-processing

For all *in-vivo* and *in-vitro* measurements, the correction of eddy currents, noise filtering (threshold: 0.07-0.2 cm/s,  $0.1 \pm 0.03$  cm/s), anti-aliasing (i.e., reconstruction of dual-VENC data), and calculation of phase-contrast MR angiograms (MRA) were performed using an in-house MATLAB tool.(47,48)

Furthermore, a semi-automatic MATLAB tool was utilised for co-registering TOF images with 4D Flow MRI data through rigid registration [functions from the SPM12 MATLAB toolbox were implemented (Statistical Parametric Mapping 12) (49)]. Vessel segmentations were determined by using intensity thresholding of the co-registered TOF images. The same segmentation binary mask was applied consistently across all three resolutions (ALR, AHR, and Super-Resolution (SR)), ensuring uniformity in the segmentation process. This is followed by labelling the intracranial vessels into left and right ICA (internal carotid artery) and left and right MCA (middle cerebral artery). Automatic equidistant analysis planes were then positioned along the centrelines of each vessel section, and direct hemodynamic parameters such as peak velocity and flow rate were extracted (refer to Fig. 2) (7,50,51). The high-resolution TOF segmentation was downsampled to match the acquired low resolution (ALR) of the 4D Flow MRI.

## 2.5. Super Resolution Conversion

The 4D Flow MRI datasets, originally acquired at a native spatial resolution of  $1.0 \times 1.0 \times 1.0$  mm<sup>3</sup> (*in-vitro*) or  $0.98-1.1 \times 0.98-1.1 \times 1.0-1.1$  mm<sup>3</sup> (*in-vivo*) underwent spatial resolution-enhancement using the publicly available deep residual network 4DFlowNet (37,52), which was previously published by Ferdian et al (37). In brief, 4DFlowNet is a deep learning model trained to generate high-resolution images from low-resolution 4D Flow MRI data, with performance specifically trained and validated for both large-vessel (aortic) (37) and small-vessel (cerebrovascular) (38,52) anatomies. For the sake of this work, weights optimised for cerebrovascular flows were utilised considering the similarity in anatomical cross-section (38).

**TABLE 1** Patient demographic information.

Subject	Age [Years]	Sex	Affected Vessel	Grade	BMI [kg/m <sup>2</sup> ]	Smoker
1	62	M	Right MCA	Mild	28.02	N
2	72	F	Right MCA	Moderate	28.70	N <sup>a</sup>
3	78	M	Right MCA	Moderate	26.05	N <sup>a</sup>
4	80	M	Right MCA	Moderate	22.61	N <sup>a</sup>
5	64	M	Left MCA	Moderate	23.73	N
6	71	M	Left ICA	Moderate	35.10	N
7	77	F	Right ICA	Severe	23.02	Y
8	69	M	Right ICA	Severe	24.18	N <sup>a</sup>
9	79	M	Right MCA	Severe	28.89	N <sup>a</sup>
10	52	M	Left MCA	Severe	27.36	N <sup>a</sup>

<sup>a</sup>Former smoker

**TABLE 2** *In-vitro* TOF, and 4D Flow Acquired Low Resolution (ALR), Acquired High Resolution (AHR), and *in-vivo* TOF and 4D Flow MRI scan parameters.

	Stenosis phantom			ICAD patients	
	TOF	ALR	AHR	TOF	4D Flow
Pixel Spacing [mm]	0.50	1.0	0.5	0.52	1.0-1.1
Slice Thickness [mm]	0.50	1.0	0.5	0.50	1.0-1.1
Cardiac Phases	-	16	13	-	8 (7-18)
Temporal resolution [ms]	-	47.6	58.1	-	42-86
TR [ms]	21.3	6.8	8.3	21	6.1-6.2
TE [ms]	5.9	4.2	5.6	3.4	3.4
FA [°]	20	15	15	17	15
VENC [cm/s]	-	50/100	50/100	-	50-60/100-120
Acceleration factor	7.2	2	2	2	5
Scan time [min]	1	30	110	4-5	10-15

Super-resolution processing of the *in-vitro* or *in-vivo* 4D Flow MRI data resulted in a doubled effective resolution (0.49-0.55 x 0.49-0.55 x 0.5-0.55 mm<sup>3</sup>) (52). The inference process of 4DFlowNet was done in Python 3.9.12 (Python Software Foundation, Beaverton, OR) using TensorFlow 2.10.0 on a 13th Gen Intel Core i7-13700 (2100 MHz, 16 Cores) CPU with an NVIDIA GeForce RTX 4070 Ti GPU with 16 GB VRAM.

## 2.6. Pressure drop estimation

Central to the functional assessment of stenotic vessels is the evaluation of trans-stenotic relative pressure. Amongst a variety of available techniques, the virtual work-energy relative pressure (vWERP) technique is a recently proposed algorithm utilising a user-defined auxiliary flow field which, in combination with the acquired flow field itself, enables interrogation of relative pressure through arbitrary vascular sections. Derived, reviewed, and validated in detail previously (33), and with vWERP having been utilised across a variety of cardiovascular compartments(17,33,38,52), this algorithm computes relative pressures by:

$$\Delta p_{\text{vWERP}} = -\frac{1}{Q_e} \cdot \left( \frac{\partial}{\partial t} K_e + A_e + V_e \right) [1]$$

where  $\Delta p$  is the relative pressure,  $Q_e$  is the virtual inflow,  $K_e$  is the virtual kinetic energy within the fluid,  $A_e$  is the rate at which kinetic energy either enters, exits, or increases within the region of interest, and  $V_e$  is the pace at which viscous energy dissipates within the fluid (see Eqs. 1 to 4) (33).

$$\frac{\partial K_e}{\partial t} = \int_{\Omega} \rho \frac{\partial v}{\partial t} \cdot w d\Omega [2]$$

$$A_e = \int_{\Omega} \rho (v \cdot \nabla v) \cdot w [3]$$

$$V_e = \int_{\Omega} \mu \nabla v : \nabla w \, d\Omega \quad [4]$$

Here,  $v$  represents the acquired fluid velocity,  $\mu$  and  $\rho$  denote the dynamic viscosity and density, respectively, and  $w$  denotes a virtual auxiliary test field, and  $\Omega$  the entire fluid domain (33). Noticeably, vWERP acts as a volumetric estimator, taking all velocity information into account from a proximal inlet to a distal outlet plane. Further,  $v$  consistently originated from the acquired 4D Flow data, with only the auxiliary field  $w$  defined as per segmentation boundaries (33).

For all evaluated vascular sections (*in-vitro* and *in-vivo*), vWERP was used to derive trans-stenotic relative pressures with vascular segmentations provided by corresponding co-registered TOF masks (see section 2.4). For the stenosis phantom, the analysis planes corresponded to the positions of the catheter measurements (refer to Fig. 1). For the *in-vivo* data, the inlet and outlet analysis planes were positioned proximal and distal to the intracranial stenosis (see Fig. 2). Segmentation from TOF imaging was utilised to position analysis planes in all cases.

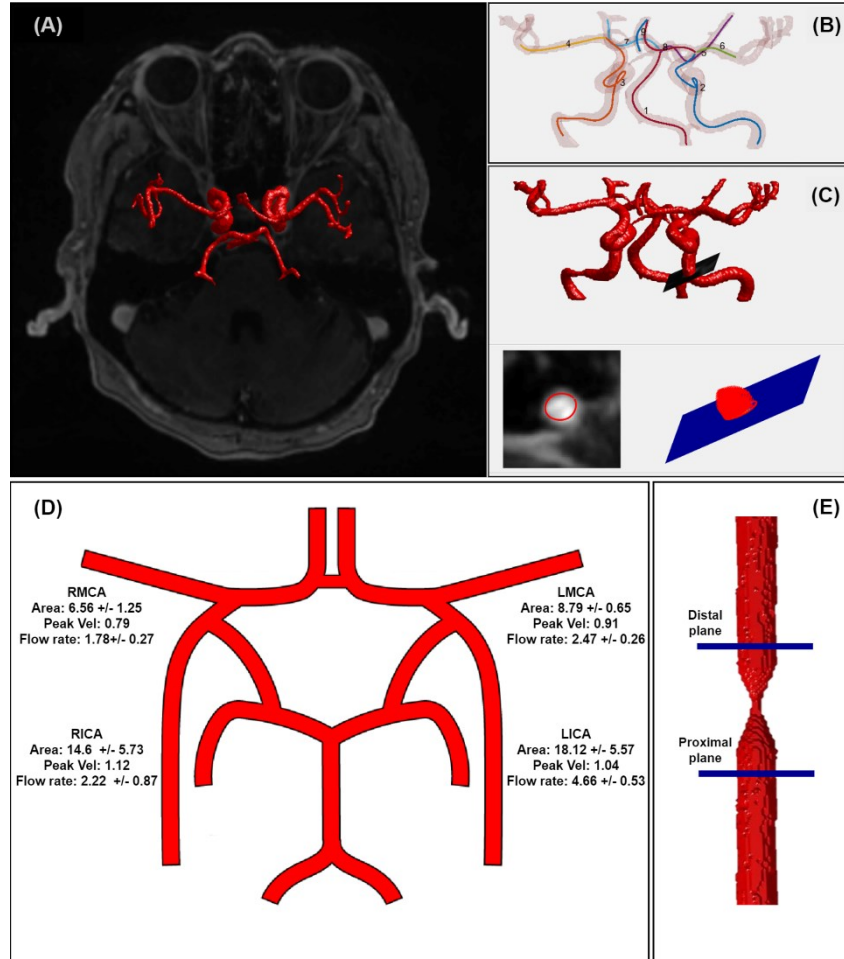


**FIGURE 2** Hemodynamic quantification which includes: (A) Threshold-based segmentation, (B) vasculature centrelines extraction, (C) Assignment of 2D analysis planes perpendicular to the centrelines, with segmentation of the vessel lumen and representation of the velocity profile across the 2D plane, (D) Schematic showing the Area, maximum peak velocity, and flow rate for major artery of the Circle of Willis (CoW), (E) Schematic diagram of the stenosis illustrating the location of vWERP inlet and outlet analysis planes, positioned proximal and distal to the stenotic region.

## 2.7. Statistics

Descriptive statistics were employed to characterise the data distribution including measures such as mean, standard deviation, median, and interquartile range. Intraclass Correlation Coefficient (ICC) and Bland-Altman analysis, were utilised to assess agreement between the data sets of different spatial resolutions (53,54).

Additionally, a paired t-test was used to compare each estimation method (AHR, SR, and ALR) with the reference catheter pressure measurements, using a significance level set at  $p < 0.05$ .

Root Mean Square Error (RMSE) was also calculated to quantify the accuracy of the *in-vitro* pressure measurements.

### 3. Results

#### 3.1. *In-vitro*

##### 3.1.1. Agreement of velocities between acquired and super-resolution

The mean flow rate determined by the Doppler ultrasound for the 50% stenosis was  $0.156 \pm 0.002$  l/min. In comparison, the flow rates determined by 4D flow MRI were  $0.178 \pm 0.006$  l/min,  $0.168 \pm 0.006$  l/min, and  $0.191 \pm 0.006$  l/min, for ALR, SR, and AHR, respectively. For the 75% stenosis, the mean flow rates were  $0.093 \pm 0.002$  l/min,  $0.101 \pm 0.004$  l/min,  $0.092 \pm 0.005$  l/min, and  $0.112 \pm 0.010$  l/min for the Doppler ultrasound, ALR, SR, and AHR, respectively.

Maximum Intensity Projection (MIP) images of the stenosis phantom derived from *in-vitro* 4D Flow MRI scans of the 50 % stenosis (A) and the 75 % stenosis (B) are presented in Figure 3. The images are arranged from left to right showing the velocity magnitude of the acquired low-resolution (1 mm), super-resolution (0.5 mm), and acquired high-resolution (0.5 mm) datasets, respectively. As observed, super-resolution conversion qualitatively de-noises the input data. Of note, the flow jet in Figure 3 was not centred in the tube. Specifically, the flexible nature of the tubing used in the phantom setup results in slight deviations from a perfectly straight and levelled positioning of the tubing for the fluid inflow, leading to a flow profile that is not perfectly centred. However, all measurements were conducted using the same experimental setup, with no modifications, to ensure comparability across the datasets.

Bland-Altman analysis of flow velocity values revealed that, for the 50 % stenosis, the limits of agreement (LOA) were  $\pm 42.4$  % of the mean value (mean bias of  $-4.9$  %) between the acquired 1 mm and 0.5 mm resolutions, compared to  $\pm 39.1$  % LOA (mean bias of  $-6.5$  %) for the super-resolved vs. acquired 0.5 mm resolution (see supporting figure S1). For the 75 % stenosis, the LOA were  $\pm 65.7$  % of the mean value (mean bias of  $-10.1$ %) between the acquired 1 mm and 0.5 mm resolutions, compared to  $\pm 54$  % LOA (mean bias of  $-6.8$  %) for the super-resolved vs. acquired 0.5 mm resolution (see supporting figure S2).

Correlation analysis showed intraclass correlation coefficients (ICC) of 68.5 for the 50% stenosis and 85.8 for the 75% stenosis between the 1 mm and acquired 0.5 mm resolutions, indicating moderate and good agreement, respectively. Meanwhile, ICCs were 75.3 for the 50% stenosis and 91.4 for the 75% stenosis for the super-resolved vs. acquired 0.5 mm resolution, indicating good and excellent agreement, respectively (see supporting figure S3).

##### 3.1.2. Pressure drop

Figure 4 illustrates the time-dependent pressure drop in millimetres of mercury (mmHg) for both stenosis channels. The vWERP pressure estimations derived from the acquired low-resolution, acquired high-resolution, and super-resolution 4D Flow data are compared to the catheter measurements. The black lines represent the temporal mean of the catheter measurements while the grey shaded areas indicate the standard deviations. Of note, the discrepancy in the number of cardiac phases between Table 2 (16 for ALR and 13 for AHR) and the plot (15 for ALR and 12 for AHR) arises from the vWERP algorithm, where the algorithm computes temporal derivatives between discrete measurement points, resulting in  $(n-1)$  output derivations for a sequence of  $n$ -acquired frames (33).

In both stenoses, underestimation was observed for the acquired low-resolution measurement relative to the catheter measurements, with the disparity being more pronounced in the 75% stenosis compared to the 50% stenosis (average difference  $-0.37 \pm 0.19$  mmHg at 50% stenosis,  $p < 0.001$ ;  $-0.95 \pm 0.16$  mmHg at 75% stenosis,  $p < 0.001$ ). These extremely low p-values indicate significant disagreement, especially in the 75% stenosis. In contrast, the acquired high-resolution measurements showed a closer agreement with the catheter measurements in both stenoses (average difference  $-0.15 \pm 0.19$  mmHg at 50% stenosis,  $p = 0.018$ ;  $-0.21 \pm 0.52$  mmHg at 75% stenosis,  $p = 0.19$ ). Although there was still some underestimation at 75% stenosis, the smaller average difference and the comparatively higher p-value suggest a more robust alignment with the catheter measurements compared to the low-resolution data. Importantly, this agreement was maintained when converting low- to super-resolution data, with similar agreements to what was observed in the high-resolution instance (average difference  $-0.21 \pm 0.26$  mmHg at 50% stenosis,  $p = 0.008$ ;  $-0.20 \pm 0.60$  mmHg at 75% stenosis,  $p = 0.22$ ).

The Bland-Altman assessment (supporting figure S4) reveals smaller biases and limits of agreement for both acquired high-resolution (AHR) and super-resolution (SR) estimations compared to the catheter measurement (Bias:  $-22.69$  % of the mean value and  $-25.54$  %, LOA:  $\pm 94.24$  % and  $\pm 113.21$  % respectively), whereas the bias and LOA for the acquired low-resolution (ALR) estimation are distinctly larger (Bias:  $-116.59$  %, LOA:  $\pm 118.85$  %), as shown in Table 3.

In addition, AHR (ICC = 0.89, Slope = 1.39,  $p = 0.012$ ) and SR (ICC = 0.86, Slope = 1.42,  $p = 0.002$ ) demonstrate good agreement with the catheter measurements, whereas ALR (ICC = 0.71, Slope = 0.53,  $p < 0.001$ ) shows moderate agreement, as detailed in Table 3.

Additionally, we calculated the Root Mean Square Error (RMSE) for the Acquired Low Resolution (ALR), Acquired High Resolution (AHR), and Super-Resolution (SR) methods, using catheter-based measurements as the reference. For the 50% stenosis, the RMSE values were 0.41 mmHg (108.67% of the mean) for ALR, 0.24 mmHg (48.43% of the mean) for AHR, and 0.32 mmHg (71.03% of the mean) for SR. For the 75% stenosis, RMSE values were 0.96 mmHg (127.80%) for ALR, 0.54 mmHg (49.09%) for AHR, and 0.64 mmHg (54.77%) for SR. Across all stenosis cases, the RMSE values were 0.74 mmHg (130.95%) for ALR, 0.42 mmHg (52.25%) for AHR, and 0.49 mmHg (62.27%) for SR.

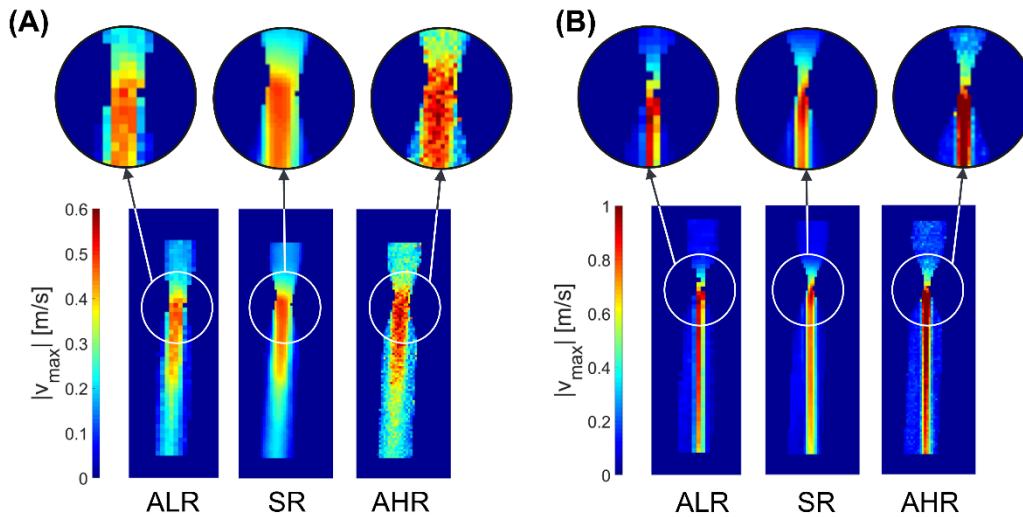


**FIGURE 3** Maximum intensity projection (MIP) images derived from 4D flow MRI of (A) the 50% stenosis, and (B), the 75% stenosis. With acquired low-resolution (ALR, 1 mm), super-resolution (SR, 0.5 mm), and acquired high-resolution (AHR, 0.5 mm) respectively, starting from the left

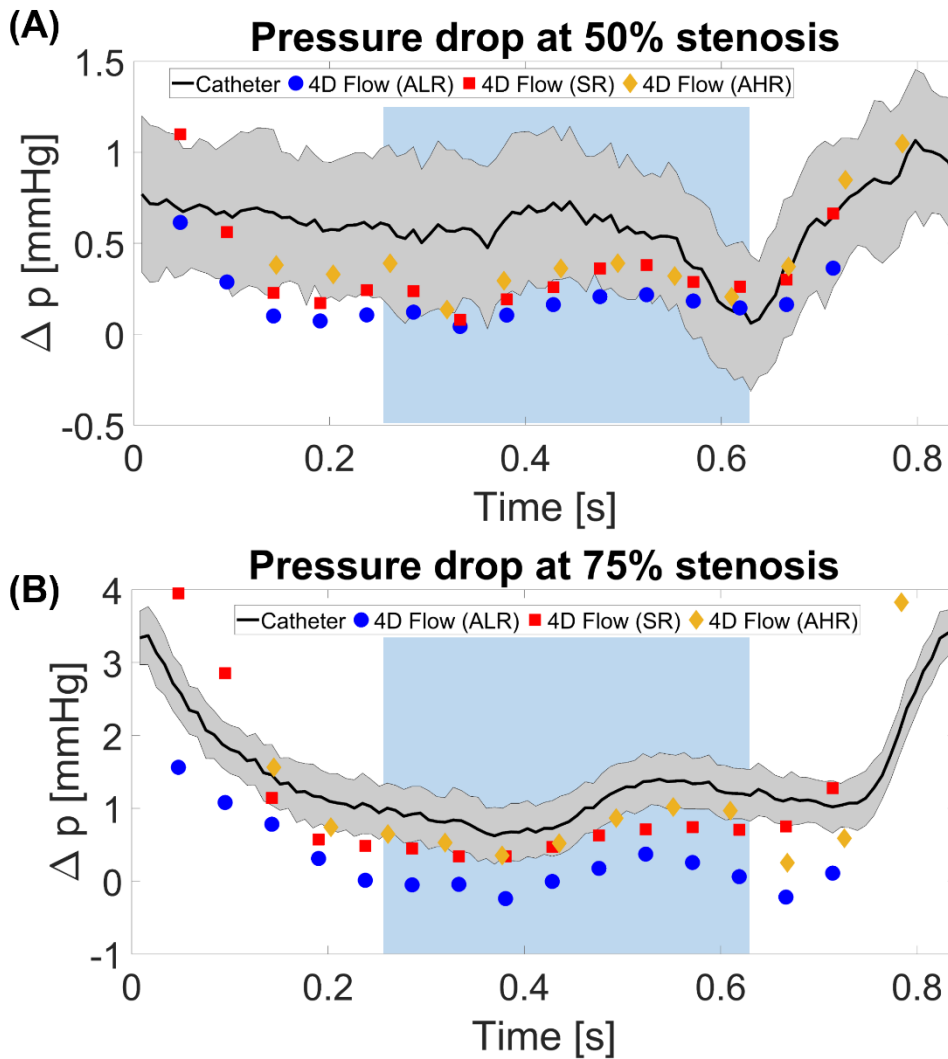


**FIGURE 4:** Pressure drop comparison in the 50 % (A), and 75 % (B) stenosis. The plots illustrate pressure catheter measurements alongside pressure estimations derived from acquired low-resolution, acquired high-resolution, and super-resolution data. The black lines represent the temporal mean of the catheter measurements while the gray shaded areas indicate the standard deviations. The blue shaded area indicates the diastole.

**TABLE 3:** Comparison of Bias (% of the mean value) and Statistical Measures between Reference Catheter Pressure measurements and Pressure Estimations using Acquired Low-Resolution (ALR), Acquired High-Resolution (AHR), and Super-Resolution (SR).

	Bias		LOA		Slope	Intercept	ICC	P
	mmHg	%	mmHg	%				
ALR	-0.66	-116.59	0.67	118.85	0.53	-0.24	0.71	<0.001
AHR	-0.18	-22.69	0.75	94.24	1.39	-0.52	0.89	0.012
SR	-0.20	-25.54	0.90	113.21	1.42	-0.58	0.86	0.002

### 3.2. In vivo

#### 3.2.1. Flow rates and peak velocities

Qualitatively, 4DFlowNet's application enhances streamline quality and congruence throughout the arterial cerebrovasculature, including the Circle of Willis as well as selected stenotic vessel sections (Figure 5).

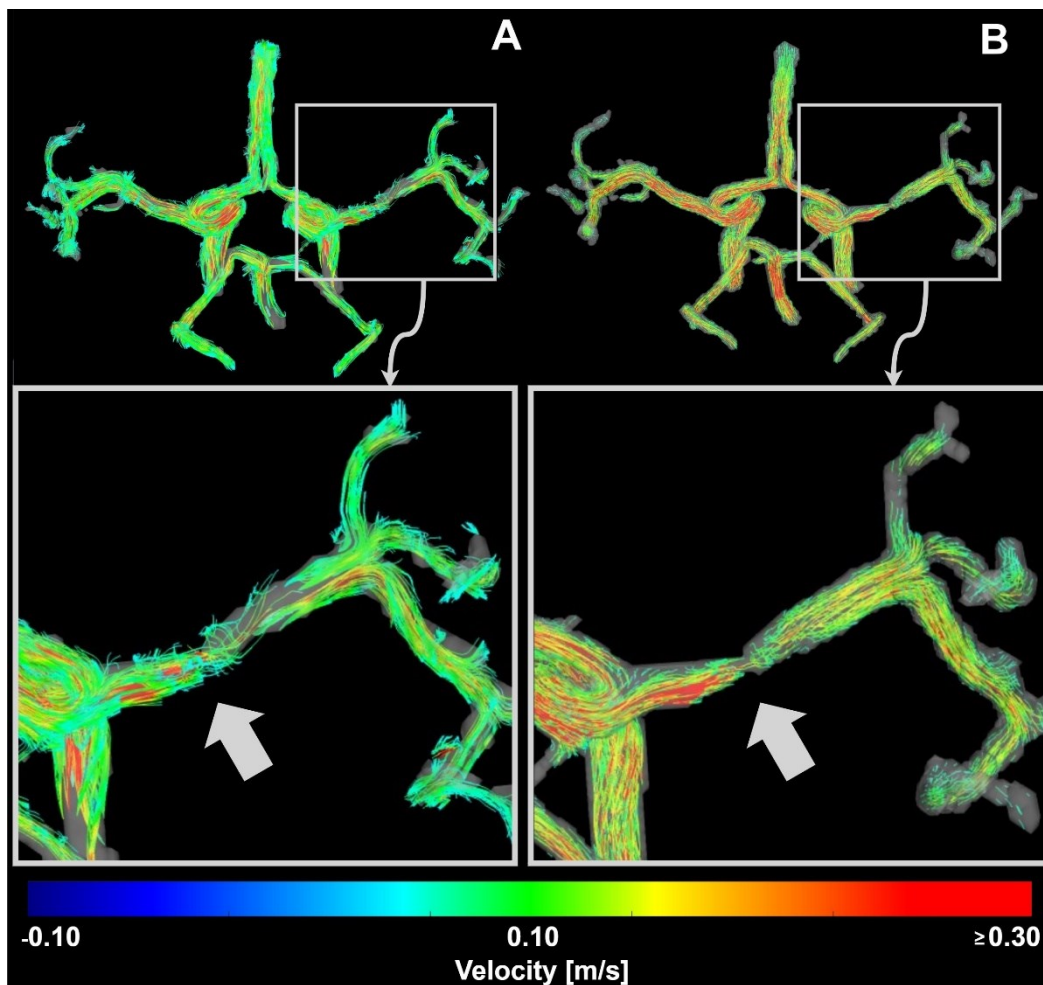


**FIGURE 5** 4D Flow MRI streamline visualisation (summation over all the time points) of a patient with severe stenosis in the MCA: (A) 1 mm isotropic Acquired resolution (AR). (B) 0.5 mm isotropic super-resolution (SR). Stenosis is marked with a grey arrow in both A and B.

Figure 6 illustrates corresponding maximum intensity projection (MIP) images of the flow velocity in stenotic vessels for each of the ten cases. These MIP images highlight the noise reduction with super-resolution (SR), regardless of stenosis severity.

The analysis of mean flow rates for acquired and super-resolution data in vessels with varying degrees of stenosis (affected vessels) revealed distinct differences in mean flow rate calculation. Particularly in vessels with severe stenosis, there is a trend of higher flow rate values with the super-resolution data (0.97 vs 0.77 ml/s, 1.63 vs 1.47 ml/s, 1.64 vs 1.39 ml/s, 4.08 vs 3.70 ml/s, 2.76 vs 2.53 ml/s, 3.95 vs 3.66 ml/s, 1.24 vs 0.98 ml/s, and 2.68 vs 2.67 ml/s) as shown in Table 4. The same can be noticed in the unaffected side (i.e., vessels contralateral to the affected vessel, such as the right MCA when the left MCA is stenotic) (2.14 vs 2.04 ml/s, 1.25 vs 1.23 ml/s, 1.23 vs 1.19 ml/s, 3.84 vs 3.42 ml/s, 4.97 vs 4.69 ml/s, 4.12 vs 1.00 ml/s, 2.03 vs 1.86 ml/s, and 1.57 vs 1.40 ml/s) with some vessels where the SR gives lower mean flow rate values (1.19 vs 1.27 ml/s, and 1.02 vs 1.37 ml/s).

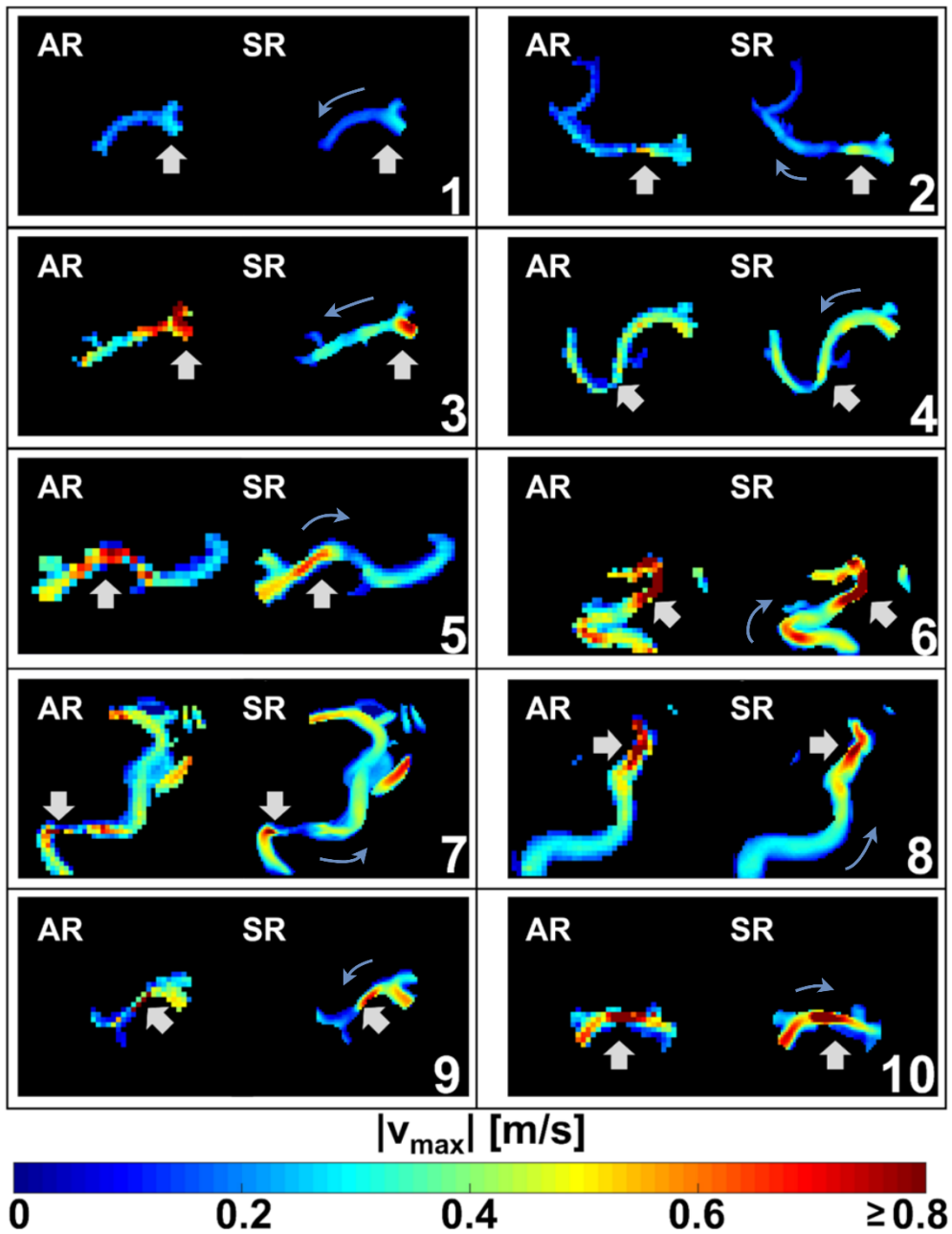


**FIGURE 6** Maximum intensity projection (MIP) images illustrating the peak velocity in stenotic vessels for each of the ten cases (see Tables 2 and 4) with both Acquired resolution (AR) and super-resolution (SR) (flow direction indicated by the blue arrows). These MIPs showcase the enhanced visualisation of stenosis (location marked with grey arrows) in the SR cases.

Regarding velocities, for some vessels on the unaffected side, the SR data shows slightly higher peak velocities than AR data (0.52 vs. 0.44 m/s, 0.63 vs. 0.56 m/s, 1.41 vs. 1.00 m/s, 1.23 vs. 1.04 m/s, 0.98 vs. 0.92 m/s, and 0.46 vs. 0.36 m/s). However, in other cases, the SR data provides lower peak velocity values (0.47 vs. 0.56 m/s, 0.43 vs. 0.53 m/s and 1.04 vs. 1.05 m/s). That can also be noted for the peak velocities on the affected side (0.30 vs. 0.28 m/s, 0.79 vs. 0.99 m/s, 0.58 vs. 1.20 m/s, 0.61 vs. 0.72 m/s, 1.07 vs. 0.97 m/s, 1.78 vs. 1.38 m/s, 1.16 vs. 1.12 m/s, 0.95 vs. 0.76 m/s, 0.97 vs. 1.17 m/s, and 1.57 vs. 1.24 m/s) (Table 4).

In summary, differences were observed between AR and SR methods across all patients, with an overall trend towards higher values with SR, and a statistically significant difference found for mean flow rate in affected vessels (AR: Median (IQR) = 1.43 (1.69) ml/s SR: Median (IQR) = 1.64 (1.67) ml/s,  $p = 0.0124$ ). No differences in flow rate in unaffected vessels and peak velocity in affected and unaffected vessels were observed. The Bland-Altman analysis (AR-SR) showed that for mean flow rate in unaffected vessels, the bias was -3.89 % of the mean value and the LOA  $\pm 17.73$  %. For peak velocity in unaffected vessels, the bias was -8.03 % with LOA  $\pm 43.30$  %. For mean flow in affected vessels, the bias was -8.05 % and the LOA was  $\pm 16.05$  %. In the case of peak velocity in affected vessels, the bias was 0.55 % with LOA  $\pm 59.15$  %.

**TABLE 4** Comparison of peak pressure drop, Mean Flow rate and Peak velocity in both affected and unaffected sides estimated using Acquired Resolution (AR), and Super Resolution (SR)

Subject	Grade	Peak Pressure Drop at stenosis [mmHg]		Affected Side				Unaffected Side			
				Mean Flow [ml/s]		Peak Velocity [m/s]		Mean Flow [ml/s]		Peak Velocity [m/s]	
		AR	SR	AR	SR	AR	SR	AR	SR	AR	SR
1	Mild MCA	0.14	0.16	0.74	0.65	0.28	0.30	1.27	1.19	0.44	0.52
2	Moderate MCA	2.81	2.95	0.77	0.97	0.99	0.79	2.04	2.14	0.56	0.63
3	Moderate MCA	1.37	1.38	1.18	1.09	1.20	0.58	1.37	1.02	0.53	0.43
4	Moderate MCA	1.11	1.44	1.47	1.63	0.72	0.61	1.23	1.25	0.56	0.47
5	Moderate MCA	1.57	2.01	1.39	1.64	0.97	1.07	1.19	1.23	0.56	0.43
6	Moderate ICA	1.55	1.98	3.70	4.08	1.38	1.78	3.42	3.84	1.00	1.41
7	Severe ICA	3.50	3.62	2.53	2.76	1.12	1.16	4.69	4.97	1.04	1.23
8	Severe ICA	2.20	3.07	3.66	3.95	0.76	0.95	4.00	4.12	0.92	0.98
9	Severe MCA	3.58	3.79	0.98	1.24	1.17	0.97	1.86	2.03	1.05	1.04
10	Severe MCA	2.90	2.88	2.67	2.68	1.24	1.57	1.40	1.57	0.36	0.46

### 3.2.2. Pressure drop

Despite the absence of *in-vivo* reference pressure data, a consistent pattern of lower pressure drop was noted at lower spatial resolution. In contrast, conversion into super-resolution images rendered an increase in pressure drop with a systematic increase compared to their lower-resolution counterparts (AR: Median (IQR) = 1.89 (1.53) mmHg vs SR: Median (IQR) = 2.45 (1.63) mmHg,  $p = 0.016$ ) as shown in Table 4 (mean difference  $0.26 \pm 0.28$  mmHg). This statistically significant behaviour was evident across various grades of stenosis severity. Moreover, Bland-Altman analysis comparing super-resolution (SR) and acquired resolution (AR) data for peak pressure drop revealed a bias of 11.60 % of the mean value with limits of agreement (LOA) of  $\pm 24.35$  %, meaning an average increase of 0.26 mmHg when converting to super-resolution imaging (see supporting figure S5).

## 4. Discussion

In this study, we assessed the effect of super-resolution 4D Flow MRI and coupled physics-informed image analysis to quantify pressure changes across intracranial atherosclerotic stenoses. As validated in a dedicated experimental setup, super-resolution image conversion effectively mitigates biases observed in low-resolution estimations of relative pressure, whilst maintaining overall performance with regards to flow rate and velocity. Further clinical implementation highlighted visual improvements with super-resolution conversion, including apparent upregulation of effective trans-stenotic pressure drop.

Of direct relevance, our results align with the findings of Ferdian et al. (38) who utilised the same combination of super-resolution imaging and vWERP-based analysis, however, predominantly doing so across non-stenosed intracranial vessel sections. As reported therein, we further confirm how super-resolution image conversion mitigates biases otherwise observed in pressure estimates at acquired  $<1$  mm resolution.

This is also consistent with preceding work by Marlevi et al. (17), where *in-silico* based analysis highlighted how non-invasive pressure drop estimations in an intracranial setting with pulsing blood flow are directly dependent on effective spatial resolution; a fact that originates from the need to accurately quantify spatial gradient terms when deriving pressure changes from imaged velocity data of narrow vascular structures. While these aforementioned studies did not specifically assess stenotic

vessel sections, our work corroborates the notion that spatial resolution is imperative for accurate image-based quantification of the cerebrovasculature. Further, our work also adds evidence to the use of super-resolution image conversion, not only in qualitatively enhancing velocity-to-noise ratios but also in enhancing our ability to quantify functional metrics of direct clinical relevance.

The Maximum Intensity Projection (MIP) images and statistical analysis for the *in-vitro* flow data revealed that the super-resolution (0.5 mm) images closely matched the acquired high-resolution (0.5 mm) images, showing improvements in the accuracy of hemodynamic parameters estimations over the acquired low-resolution (1 mm) images. Notably, Bland-Altman and ICC analyses highlighted how agreement with reference high-resolution velocities was more evident in the more severe 75 % stenosis cases as compared to the milder 50 % stenosis cases. Conversely, when moving into derivations of pressure changes, no apparent difference was observed between the 50 and 75 % stenosis cases, where super-resolution image conversion showed to be equally successful in mitigating biases otherwise observed in the low-resolution input data (again in conformance with the findings of Marlevi et al(33)). Root Mean Square Error (RMSE) values were calculated to assess the accuracy of non-invasive pressure measurements compared to the catheter-based reference. The results demonstrated that both AHR and SR consistently yielded lower RMSE values than ALR, confirming their superior accuracy in pressure drop estimation. While AHR provided the most precise measurements, SR achieved RMSE values close to AHR, significantly reducing errors relative to ALR.

Moving into the *in-vivo* data, super-resolution imaging rendered an apparent increase in derived pressure drops. This pattern was observed across different levels of stenosis severity, where an increase in pressure drop as a function of increased degrees of stenosis is in agreement with the notion of regional mass conservation, as well as previous experimental findings (7). Whereas lacking high-resolution reference data, qualitative assessment of streamline visualisations and MIP images for the *in-vivo* cohort underlines the visual improvement in image quality achieved by super-resolution processing, possibly facilitating improved visualisation of regional vascular structures and flow patterns in future clinical research extensions.

One limitation of this study is the relatively small size of the *in-vivo* cohort, which may affect the generalizability of the findings to broader patient populations. Future studies with larger patient cohorts are therefore warranted. Also, the patient cohort study was retrospective, as the patients had been previously scanned for another study, and we only obtained the data for post-processing which limits control over scan parameters and patient selection. While GRAPPA-accelerated dual-VENC 4D Flow MRI (R=2) was used for *in-vitro* experiments, because there was no time limitation, it is impractical for routine *in-vivo* imaging. Therefore, in this study, the *in-vivo* data was acquired with kt-GRAPPA acceleration (R=5). Using different methods of acceleration for *in-vivo* and *in-vitro*, however, did not affect our results, as comparisons were made only within the *in-vitro* or *in-vivo* datasets, without direct comparison between the two groups. Additionally, differences in temporal resolution between AHR and ALR may have contributed to alignment issues between pressure curves and to systematic errors when comparing the velocity values for the different resolution settings. In addition, the lower temporal resolution of MR scans affects the shape of the curves, resulting in imperfect co-registration with the catheter measurements. The comparison with the catheter pressure measurement required additional processing and alignment with the MRI data because of the MRI-incompatible nature of the setup. Noticeable, the pressure curves were averaged over 10 cycles ( $\approx 8$  seconds), being shorter than the MRI acquisition. This was deemed sufficient, due to the high reliability of the used pump, as verified by ultrasonic flow sensors over extended periods in a previous experiment and confirmed through calibration according to the manufacturer's instructions.

Additionally, the pressure catheters used are subject to time-dependent drift. While the drift over 12 hours is minimal and the recommended usage time is up to 3 hours, we limited the catheter usage to a shorter duration to minimise any potential drift effects. Lastly, another limitation was the absence of *in-vivo* catheter-based reference data for pressure measurements in brain clinical intracranial vessels limiting direct clinical translational of our derived results.

Finally, super-resolution techniques such as the one used in our study bear specific clinical relevance in being able to enhance spatial resolution *post-scan*, mitigating the need for altered clinical protocols, increased scan times, or adjusted signal-to-noise ratio. Whilst still very much a research tool, the translation of these utilities into a clinical research setting is hence comparably easy, with several works now testing the capabilities of trained neural networks in a clinical research setting (35–38,55). Our study adds to this body of work, highlighting in particular how super-resolution imaging allows for direct, non-invasive access of intracranial relative pressure – an estimate of proven clinical relevance in other vascular domains, and where non-invasive quantification tools now open for a variety of future clinical application areas.

## 5. Conclusions

In this study, we have shown how super-resolution 4D Flow MRI and coupled physics-informed image analysis successfully enable the non-invasive estimation of intracranial pressure drops across stenotic vessels with pulsing blood flow. Our findings were experimentally validated in a dedicated *in-vitro* experimental setup. Further, clinical utility has been exemplified by *in-vivo* implementation in an intracranial atherosclerotic pilot cohort, highlighting changes observed by super-resolution image conversion. Whilst extended patient studies and *in-vivo* validations could add further evidence to the above, our work showcases the potential of advanced hemodynamic imaging in extracting pressure changes through previously inaccessible trans-stenotic vessel sections.

**Author contributions:** AeA: Data curation, Formal analysis, Investigation, Methodology, Validation, Visualization, Writing - original draft. SuS: Conceptualization, Formal analysis, Funding acquisition, Investigation, Methodology, Project administration, Software, Supervision, Validation, Visualization, Writing - original draft, Writing - review & editing. SA: Formal analysis, Investigation, Project administration, Resources, Supervision, Validation, Writing - review & editing. RA: Data curation, Formal analysis, Investigation, Writing - review & editing. AV: Data curation, Software, Writing - review & editing. MA: Software, Writing - review & editing. MM: Funding acquisition, Project administration, Resources, Supervision, Writing - review & editing. PW: Conceptualization, Data curation, Formal analysis,

Investigation, Methodology, Project administration, Software, Supervision, Validation, Visualization, Writing - review & editing. DM: Conceptualization, Funding acquisition, Methodology, Project administration, Software, Supervision, Validation, Writing - review & editing.

**Acknowledgements:** The authors would like to thank the entire research group of the Department of Medical Physics at the University of Greifswald for their support. References.

**Sources of Funding:** Views and opinions expressed are those of the authors and do not reflect those of the European Union or the European Research Council Executive Agency. DM acknowledges funding from the European Union (ERC, MultiPRESS, 101075494). SuS and PW acknowledge funding from the United States of America from the National Heart, Lung and Blood Institute: 1R01HL149787, National Institute of Neurological Disorders and Stroke: 5R21NS122511. The University of Greifswald received funding from the German Research Council (DFG INST 292/155-1 FUGG).

**Ethics Statement** The studies involving human participants were approved by the Institutional Review Board Office at Northwestern University. They were conducted following local legislation and institutional guidelines. Written informed consent was obtained from all participants. The stenosis cases were retrospectively selected.

**Competing interests:** The authors declare that the research was conducted without any commercial or financial relationships that could be construed as a potential conflict of interest. Dr. Alireza Vali's involvement in the study was during his affiliation with the Department of Radiology, Northwestern University, Feinberg School of Medicine, Chicago, IL, United States. He is currently employed by Qualcomm Technologies, Inc., San Diego, California, USA. However, his role in this research was independent of his current employment, and no commercial or financial interests from Qualcomm were involved. Dr. Vali provided a critical manuscript review in a personal capacity unrelated to his role at Qualcomm Technologies.

**Data availability statement:** The in vivo datasets presented in this article are restricted because datasets from an IRB-approved study involving patients were used. Requests for the de-identified data should be made to Abby Hagler (abby.hagler@northwestern.edu) at Northwestern University. She will coordinate the data sharing process with the investigators and the NU Office of Sponsored Research.

The in vitro datasets and source code for the 4DFlowNet are available as electronic supplementary material.

## References

1. Suri MFK, Johnston SC. 2009. Epidemiology of intracranial stenosis. *J. Neuroimaging* 19, 115–16S. (10.1111/j.1552-6569.2009.00415.x) - [DOI](#)
2. Bae HJ, Lee J, Park JM, Kwon O, Koo JS, Kim BK, Pandey DK. 2007. Risk factors of intracranial cerebral atherosclerosis among asymptomatics. *Cerebrovasc. Dis.* 24, 355–360. (10.1159/000106982) - [DOI](#)
3. Chimowitz MI, et al. . 2003. Design, progress and challenges of a double-blind trial of warfarin versus aspirin for symptomatic intracranial arterial stenosis. *Neuroepidemiology* 22, 106–117. (10.1159/000068744) - [DOI](#)
4. Leng X, Wong KS, Liebeskind DS. 2014. Evaluating intracranial atherosclerosis rather than intracranial stenosis. *Stroke* 45, 645–651. (10.1161/strokeaha.113.002491) - [DOI](#) - [PMC](#)
5. Ha H, Lantz J, Ziegler M, Casas B, Karlsson M, Dyverfeldt P, Ebbers T. 2017. Estimating the irreversible pressure drop across a stenosis by quantifying turbulence production using 4D flow MRI. *Sci. Rep.* 7, 46618. (10.1038/srep46618) - [DOI](#) - [PMC](#)
6. Avery MB, Sambrano S, Khader Eliyas J, Eesa M, Mitha AP. 2018. Accuracy and precision of venous pressure measurements of endovascular microcatheters in the setting of dural venous sinus stenosis. *J. Neurointerv. Surg.* 10, 387–390. (10.1136/neurintsurg-2017-013155) - [DOI](#)
7. Vali A, Aristova M, Vakili P, Abdalla R, Prabhakaran S, Markl M, Ansari SA, Schnell S. 2019. Semi-automated analysis of 4D flow MRI to assess the hemodynamic impact of intracranial atherosclerotic disease. *Magn. Reson. Med.* 82, 749–762. (10.1002/mrm.27747) - [DOI](#) - [PMC](#)
8. Smith SC, Antman EM, Sidney Smith CC, Chair Ted Feldman VE, Hirshfeld JW, Jacobs AK. 2006. Guideline update for percutaneous coronary intervention. A report of the American College of Cardiology/American Heart Association Task Force on Practice Guidelines (ACC/AHA/SCAI Writing Committee to update the 2001 guidelines for percutaneous coronary intervention).
9. Vitiello R, McCrindle BW, Nykanen D, Freedom RM, Benson LN. 1998. Complications associated with pediatric cardiac catheterization. *J. Am. Coll. Cardiol.* 32, 1433–1440. (10.1016/s0735-1097(98)00396-9) - [DOI](#)
10. Wyman RM, Safian RD, Portway V, Skillman JJ, McKay RG, Baim DS. 1988. Current complications of diagnostic and therapeutic cardiac catheterization. *J. Am. Coll. Cardiol.* 12, 1400–1406. (10.1016/s0735-1097(88)80002-0) - [DOI](#)
11. Han YF, et al. 2016. Severity assessment of intracranial large artery stenosis by pressure gradient measurements: a feasibility study. *Catheter. Cardiovasc. Interv.* 88, 255–261. (10.1002/ccd.26414) - [DOI](#)
12. Miao Z, et al. 2016. Fractional flow assessment for the evaluation of intracranial atherosclerosis: a feasibility study. *Interv. Neurol.* 5, 65–75. (10.1159/000444333) - [DOI](#) - [PMC](#)
13. Stamm RB, Martin RP. 1983. Quantification of pressure gradients across stenotic valves by Doppler ultrasound. *J. Am. Coll. Cardiol.* 2, 707–718. (10.1016/s0735-1097(83)80311-8) - [DOI](#)
14. Donati F, Myerson S, Bissell MM, Smith NP, Neubauer S, Monaghan MJ. 2017. Beyond Bernoulli: improving the accuracy and precision of noninvasive estimation of peak pressure drops. *Circ. Cardiovasc. Imaging* 10, e005207. (10.1161/CIRCIMAGING.116.005207) - [DOI](#) - [PMC](#)
15. Baumgartner H, Stefenelli T, Niederberger J, Schima H, Maurer G. 1999. "Overestimation" of catheter gradients by Doppler ultrasound in patients with aortic stenosis: a predictable manifestation of pressure recovery. *J. Am. Coll. Cardiol.* 33, 1655–1661. (10.1016/s0735-1097(99)00066-2) - [DOI](#)
16. Garcia D, Dumesnil JG, Durand LG, Kadem L, Pibarot P. 2003. Discrepancies between catheter and Doppler estimates of valve effective orifice area can be predicted from the pressure recovery phenomenon: practical implications with regard to quantification of aortic stenosis severity. *J. Am. Coll. Cardiol.* 41, 435–442. (10.1016/s0735-1097(02)02764-x) - [DOI](#)
17. Marlevi D, et al. 2021. Noninvasive quantification of cerebrovascular pressure changes using 4D flow MRI. *Magn. Reson. Med.* 86, 3096–3110. (10.1002/mrm.28928) - [DOI](#) - [PMC](#)
18. Kirsch JD, Mathur M, Johnson MH, Gowthaman G, Scoutt LM. 2013. Advances in transcranial Doppler US: imaging ahead. *RadioGraphics* 33, E1–E14. (10.1148/rg.331125071) - [DOI](#)
19. Wagshul ME, Eide PK, Madsen JR. 2011. The pulsating brain: a review of experimental and clinical studies of intracranial pulsatility. *Fluids Barriers CNS* 8, 5. (10.1186/2045-8118-8-5) - [DOI](#) - [PMC](#)
20. Almudayni A, Alharbi M, Chowdhury A, Ince J, Alablani F, Minhas JS, Lecchini-Visintini A, Chung EML. 2023. Magnetic resonance imaging of the pulsing brain: a systematic review. *Magn. Reson. Mater. Phys. Biol. Med.* 36, 3–14. (10.1007/s10334-022-01043-1) - [DOI](#) - [PMC](#)
21. Stankovic Z, Allen BD, Garcia J, Jarvis KB, Markl M. 2014. 4D flow imaging with MRI. *Cardiovasc. Diagn. Ther.* 4, 173–192. (10.3978/j.issn.2223-3652.2014.01.02) - [DOI](#) - [PMC](#)
22. Markl M, Frydrychowicz A, Kozerke S, Hope M, Wieben O. 2012. 4D flow MRI. *J. Magn. Reson. Imaging* 36, 1015–1036. (10.1002/jmri.23556) - [DOI](#)

23. Bock J, et al. 2011. In vivo noninvasive 4D pressure difference mapping in the human aorta: phantom comparison and application in healthy volunteers and patients. *Magn. Reson. Med.* 66, 1079–1088. (10.1002/mrm.22907) - [DOI](#)
24. Tyszka JM, Laidlaw DH, Asa JW, Silverman JM. 2000. Three-dimensional, time-resolved (4D) relative pressure mapping using magnetic resonance imaging. *J. Magn. Reson. Imaging* 12, 321–329. (10.1002/1522-2586(200008)12:2<321::AID-JMRI15>3.0.CO;2-2) - [DOI](#)
25. Ebbers T, Wigström L, Bolger AF, Engvall J, Karlsson M. 2001. Estimation of relative cardiovascular pressures using time-resolved three-dimensional phase contrast MRI. *Magn. Reson. Med.* 45, 872–879. (10.1002/mrm.1116) - [DOI](#)
26. Lum DP, Johnson KM, Paul RK, Turk AS, Consigny DW, Grinde JR, Mistretta CA, Grist TM. 2007. Transstenotic pressure gradients: measurement in swine—retrospectively ECG-gated 3D phase-contrast MR angiography versus endovascular pressure-sensing guidewires. *Radiology* 245, 751–760. (10.1148/radiol.2453061946) - [DOI](#)
27. Krittian SBS, et al. 2012. A finite-element approach to the direct computation of relative cardiovascular pressure from time-resolved MR velocity data. *Med. Image Anal.* 16, 1029–1037. (10.1016/j.media.2012.04.003) - [DOI](#) - [PMC](#)
28. Riesenkampff E, Fernandes JF, Meier S, Goubergrits L, Kropf S, Schubert S, Berger F, Hennemuth A, Kuehne T. 2014. Pressure fields by flow-sensitive, 4D, velocity-encoded CMR in patients with aortic coarctation. *JACC Cardiovasc. Imaging* 7, 920–926. (10.1016/j.jcmg.2014.03.017) - [DOI](#)
29. Lamata P, et al. 2014. Aortic relative pressure components derived from four-dimensional flow cardiovascular magnetic resonance. *Magn. Reson. Med.* 72, 1162–1169. (10.1002/mrm.25015) - [DOI](#) - [PMC](#)
30. Donati F, Figueroa CA, Smith NP, Lamata P, Nordsletten DA. 2015. Non-invasive pressure difference estimation from PC-MRI using the work-energy equation. *Med. Image Anal.* 26, 159–172. (10.1016/j.media.2015.08.012) - [DOI](#) - [PMC](#)
31. Bertoglio C, Nuñez R, Galarce F, Nordsletten D, Osses A. 2018. Relative pressure estimation from velocity measurements in blood flows: state-of-the-art and new approaches. *Int. J. Numer. Method. Biomed. Eng.* 34, e2925. (10.1002/cnm.2925) - [DOI](#)
32. Švihlová H, Hron J, Málek J, Rajagopal KR, Rajagopal K. 2016. Determination of pressure data from velocity data with a view toward its application in cardiovascular mechanics. Part 1. Theoretical considerations. *Int. J. Eng. Sci.* 105, 108–127. (10.1016/j.ijengsci.2015.11.002) - [DOI](#)
33. Marlevi D, et al. 2019. Estimation of cardiovascular relative pressure using virtual work-energy. *Sci. Rep.* 9, 1375. (10.1038/s41598-018-37714-0) - [DOI](#) - [PMC](#)
34. Rutkowski DR, Roldán-Alzate A, Johnson KM. 2021. Enhancement of cerebrovascular 4D flow MRI velocity fields using machine learning and computational fluid dynamics simulation data. *Sci. Rep.* 11, 10240. (10.1038/s41598-021-89636-z) - [DOI](#) - [PMC](#)
35. Fathi MF, Perez-Raya I, Baghaie A, Berg P, Janiga G, Arzani A, D'Souza RM. 2020. Super-resolution and denoising of 4D-flow MRI using physics-informed deep neural nets. *Comput. Methods Programs Biomed.* 197, 105729. (10.1016/j.cmpb.2020.105729) - [DOI](#)
36. Nath R, Kazemi A, Callahan S, Stoddard MF, Amini AA. 2023. 4Dflow-VP-Net: a deep convolutional neural network for noninvasive estimation of relative pressures in stenotic flows from 4D flow MRI. *Magn. Reson. Med.* 90, 2175–2189. (10.1002/mrm.29791) - [DOI](#) - [PMC](#)
37. Ferdian E, Suinesiaputra A, Dubowitz DJ, Zhao D, Wang A, Cowan B, Young AA. 2020. 4DFlowNet: super-resolution 4D flow MRI using deep learning and computational fluid dynamics. *Front. Phys.* 8, 138. (10.3389/fphy.2020.00138) - [DOI](#)
38. Ferdian E, Marlevi D, Schollenberger J, Aristova M, Edelman ER, Schnell S, Figueroa CA, Nordsletten DA, Young AA. 2023. Cerebrovascular super-resolution 4D Flow MRI—sequential combination of resolution enhancement by deep learning and physics-informed image processing to non-invasively quantify intracranial velocity, flow, and relative pressure. *Med. Image Anal.* 88, 102831. (10.1016/j.media.2023.102831) - [DOI](#)
39. Summers PE, Holdsworth DW, Nikolov HN, Rutt BK, Drangova M. 2005. Multisite trial of MR flow measurement: phantom and protocol design. *J. Magn. Reson. Imaging* 21, 620–631. (10.1002/jmri.20311) - [DOI](#)
40. Samuels OB, Joseph GJ, Lynn MJ, Smith HA, Chimowitz MI. 2000. A standardized method for measuring intracranial arterial stenosis. *AJNR Am. J. Neuroradiol.* 21, 643–646. - [PMC](#)
41. Lorenz R, Bock J, Snyder J, Korvink JG, Jung BA, Markl M. 2014. Influence of eddy current, Maxwell and gradient field corrections on 3D flow visualization of 3D CINE PC-MRI data. *Magn. Reson. Med.* 72, 33–40. (10.1002/mrm.24885) - [DOI](#) - [PMC](#)
42. de Vecchi A, Clough RE, Gaddum NR, Rutten MCM, Lamata P, Schaeffter T, Nordsletten DA, Smith NP. 2014. Catheter-induced errors in pressure measurements in vessels: an in-vitro and numerical study. *IEEE Trans. Biomed. Eng.* 61, 1844–1850. (10.1109/tbme.2014.2308594) - [DOI](#) - [PMC](#)
43. Winter P, Kampf T, Helluy X, Gutjahr FT, Meyer CB, Rommel E, Bauer WR, Jakob PM, Herold V. 2013. Fast retrospectively triggered local pulse-wave velocity measurements in mice with CMR-microscopy using a radial trajectory. *J. Cardiovasc. Magn. Reson.* 15, 88. (10.1186/1532-429x-15-88) - [DOI](#) - [PMC](#)
44. Winter P, Anđelović K, Kampf T, Gutjahr FT, Heidenreich J, Zerneck A, Bauer WR, Jakob PM, Herold V. 2019. Fast self-navigated wall shear stress measurements in the murine aortic arch using radial 4D-phase contrast cardiovascular magnetic resonance at 17.6 T. *J. Cardiovasc. Magn. Reson.* 21, 64. (10.1186/s12968-019-0566-z) - [DOI](#) - [PMC](#)
45. Buck JR, Daniel MM, Singer AC. 2002. Computer explorations in signals and systems using MATLAB®. 2nd Edition. Upper Saddle River, NJ: Prentice Hall.
46. Stoica P, Moses R. 2005. Spectral analysis of signals. Upper Saddle River, NJ: Pearson Education.
47. Schnell S, et al. 2017. Accelerated dual-VENC 4D flow MRI for neurovascular applications. *J. Magn. Reson. Imaging* 46, 102–114. (10.1002/jmri.25595) - [DOI](#) - [PMC](#)
48. Bock J, Kreher BW, Hennig J, Markl M. 2007. Optimized pre-processing of time-resolved 2D and 3D phase contrast MRI data. In Proc. 15th Annual Meeting of ISMRM, Berlin, Germany, abstract 3138.
49. Ashburner J, Friston KJ. 2005. Unified segmentation. *NeuroImage* 26, 839–851. (10.1016/j.neuroimage.2005.02.018) - [DOI](#)
50. Winter P, et al. 2024. Automated intracranial vessel segmentation of 4D flow MRI data in patients with atherosclerotic stenosis using a convolutional neural network. *Front. Radiol.* 4, 1385424. (10.3389/fradi.2024.1385424) - [DOI](#) - [PMC](#)
51. Aristova M, et al. 2019. Standardized evaluation of cerebral arteriovenous malformations using flow distribution network graphs and dual-venc 4D flow MRI. *J. Magn. Reson. Imaging* 50, 1718–1730. (10.1002/jmri.26992) - [DOI](#) - [PMC](#)
52. Winter P, et al. 2023. Super-resolution assessment of relative pressure in intracranial atherosclerosis using ML-enhanced 4D flow MRI. In 2023 ISMRM & ISMRT Annual Meeting, Toronto, Canada, 3–8 June 2023, abstract 0783. (10.58530/2023/0783) - [DOI](#)
53. Shrout PE, Fleiss JL. 1979. Intraclass correlations: uses in assessing rater reliability. *Psychol. Bull.* 86, 420–428. (10.1037/0033-2909.86.2.420) - [DOI](#)
54. Bland JM, Altman DG. 2010. Statistical methods for assessing agreement between two methods of clinical measurement. *Int. J. Nurs. Stud.* 47, 931–936. (10.1016/j.ijnurstu.2009.10.001) - [DOI](#)
55. Ericsson L, et al. 2024. Generalized super-resolution 4D Flow MRI—using ensemble learning to extend across the cardiovascular system. *IEEE J. Biomed. Health Inform.* 28, 7239–7250. (10.1109/JBHI.2024.3429291) - [DOI](#) - [PMC](#)